Photoacoustic ophthalmoscopy for *in vivo* retinal imaging

Shuliang Jiao,[1,5] **Minshan Jiang,**[1] **Jianming Hu,**[1] **Amani Fawzi,**[1] **Qifa Zhou,**[2] **K. Kirk Shung,**[2] **Carmen A. Puliafito,**[1] **and Hao F. Zhang**[3,4]

[1] *Department of Ophthalmology, Keck School of Medicine, University of Southern California, Los Angeles, CA 90033, USA*

[2] *Department of Biomedical Engineering, University of Southern California, Los Angeles, CA 90033, USA*

[3] *Department of Electrical Engineering and Computer Science, University of Wisconsin-Milwaukee, Milwaukee WI 53201, USA*

[4] *zhang25@uwm.edu*

[5] *sjiao@usc.edu*

Abstract: We have developed a non-invasive photoacoustic ophthalmoscopy (PAOM) for *in vivo* retinal imaging. PAOM detects the photoacoustic signal induced by pulsed laser light shined onto the retina. By using a stationary ultrasonic transducer in contact with the eyelids and scanning only the laser light across the retina, PAOM provides volumetric imaging of the retinal micro-vasculature and retinal pigment epithelium at a high speed. For B-scan frames containing 256 A-lines, the current PAOM has a frame rate of 93 Hz, which is comparable with state-of-the-art commercial spectral-domain optical coherence tomography (SD-OCT). By integrating PAOM with SD-OCT, we further achieved OCT-guided PAOM, which can provide multi-modal retinal imaging simultaneously. The capabilities of this novel technology were demonstrated by imaging both the microanatomy and microvasculature of the rat retina *in vivo*.

©2010 Optical Society of America

OCIS codes: (110.5120) Photoacoustic imaging; (170.4500) Optical coherence tomography; (170.4470) Ophthalmology.

References and links

1. F. C. Delori, E. S. Gragoudas, R. Francisco, and R. C. Pruett, "Monochromatic Ophthalmoscopy and Fundus Photography," Arch. Ophthalmol. **5**, 861–868 (1977).
2. G. A. Williams, I. U. Scott, J. A. Haller, A. M. Maguire, D. Marcus, H. R. McDonald; "Single-field fundus photography for diabetic retinopathy screening: a report by the American Academy of Ophthalmology," Ophthalmology **111**(5), 1055–1062 (2004).
3. R. H. Webb AND G. W. Hughes, "Scanning laser ophthalmoscope," IEEE Trans. Biomed. Eng, BME **28**, 488–492 (1981).
4. D. Huang, E. A. Swanson, C. P. Lin, J. S. Schuman, W. G. Stinson, W. Chang, M. R. Hee, T. Flotte, K. Gregory, C. A. Puliafito, and J. G. Fujimoto, "Optical coherence tomography," Science **254**(5035), 1178–1181 (1991).
5. A. F. Fercher, C. K. Hitzenberger, G. Kamp, and S. Y. El-Zaiat, "Measurement of intraocular distances by backscattering spectral interferometry," Opt. Commun. **117**(1-2), 43–48 (1995).
6. M. Wojtkowski, R. Leitgeb, A. Kowalczyk, T. Bajraszewski, and A. F. Fercher, "*In vivo* human retinal imaging by Fourier domain optical coherence tomography," J. Biomed. Opt. **7**(3), 457–463 (2002).
7. N. A. Nassif, B. Cense, B. H. Park, M. C. Pierce, S. H. Yun, B. E. Bouma, G. J. Tearney, T. C. Chen, and J. F. de Boer, "*In vivo* high-resolution video-rate spectral-domain optical coherence tomography of the human retina and optic nerve," Opt. Express **12**(3), 367–376 (2004), http://www.opticsexpress.org/abstract.cfm?URI=OPEX-12-3-367.
8. M. Ruggeri, H. Wehbe, S. Jiao, G. Gregori, M. E. Jockovich, A. Hackam, Y. Duan, and C. A. Puliafito, "*In vivo* three-dimensional high-resolution imaging of rodent retina with spectral-domain optical coherence tomography," Invest. Ophthalmol. Vis. Sci. **48**(4), 1808–1814 (2007).
9. A. Harris, R. B. Dinn, L. Kagemann, and E. Rechtman, "A review of methods for human retinal oximetry," Ophthal. Surg. Las. Im. **34**, 152–164 (2003).
10. M. Hammer, S. Leistritz, L. Leistritz, and D. Schweitzer, "Light paths in retinal vessel oxymetry," IEEE Trans. Biomed. Eng. **48**(5), 592–598 (2001).

11. J. Cai, and M. Boulton, "The pathogenesis of diabetic retinopathy: old concepts and new questions," Eye (Lond) **16**(3), 242–260 (2002).
12. O. Strauss, "The retinal pigment epithelium in visual function," Physiol. Rev. **85**(3), 845–881 (2005).
13. A. von Rückmann, F. W. Fitzke, and A. C. Bird, "Distribution of fundus autofluorescence with a scanning laser ophthalmoscope," Br. J. Ophthalmol. **79**(5), 407–412 (1995).
14. H. F. Zhang, K. Maslov, and L. V. Wang, "*In vivo* imaging of subcutaneous structures using functional photoacoustic microscopy," Nat. Protoc. **2**(4), 797–804 (2007).
15. H. F. Zhang, K. Maslov, G. Stoica, and L. V. Wang, "Functional photoacoustic microscopy for high-resolution and noninvasive *in vivo* imaging," Nat. Biotechnol. **24**(7), 848–851 (2006).
16. K. Maslov, H. F. Zhang, S. Hu, and L. V. Wang, "Optical-resolution photoacoustic microscopy for *in vivo* imaging of single capillaries," Opt. Lett. **33**(9), 929–931 (2008).
17. Z. Xie, S. Jiao, H. F. Zhang, and C. A. Puliafito, "Laser-scanning optical-resolution photoacoustic microscopy," Opt. Lett. **34**(12), 1771–1773 (2009).
18. S. Jiao, Z. Xie, H. F. Zhang, and C. A. Puliafito, "Simultaneous multimodal imaging with integrated photoacoustic microscopy and optical coherence tomography," Opt. Lett. **34**(19), 2961–2963 (2009).
19. H. F. Zhang, J. Wang, Q. Wei, T. Liu, S. Jiao, and C. A. Puliafito, "Collecting back-reflected photons in photoacoustic microscopy," Opt. Express **18**(2), 1278–1282 (2010), http://www.opticsinfobase.org/oe/abstract.cfm?uri=oe-18-2-1278.
20. S. Jiao, R. Knighton, X. Huang, G. Gregori, and C. Puliafito, "Simultaneous acquisition of sectional and fundus ophthalmic images with spectral-domain optical coherence tomography," Opt. Express **13**(2), 444–452 (2005), http://www.opticsinfobase.org/abstract.cfm?URI=oe-13-2-444.
21. H. F. Zhang, K. Maslov, and L. V. Wang, "Automatic algorithm for skin profile detection in photoacoustic microscopy," J. Biomed. Opt. **14**(2), 024050 (2009).
22. American National Standard for Safe Use of Lasers ANSI Z136, 1–2007. (American National Standards Institute Inc., New York, NY, 2007).
23. H. F. Zhang, K. Maslov, M. Sivaramakrishnan, G. Stoica, and L. V. Wang, "Imaging of hemoglobin oxygen saturation variations in single vessels in vivo using photoacoustic microscopy," Appl. Phys. Lett. **90**(5), 053901 (2007).

1. Introduction

Retinal diseases are the major causes of blindness in developed countries. The accurate diagnosis and management of retinal diseases highly depend on non-invasive imaging techniques. Most of the existing retinal imaging modalities, such as fundus photography [1,2], scanning laser ophthalmoscope (SLO) [3], and optical coherence tomography (OCT) [4–8] are optical reflection based—they rely on the back-reflected light from the retinal tissues to form an image. Various contrasts such as optical scattering, Doppler shift induced by blood flow, and optical polarization have been used for both anatomical and functional ophthalmic imaging; however, until now, there still lacks an ophthalmic imaging modality that can image the optical absorption properties of retinal tissues.

Imaging the optical absorption properties at multiple wavelengths can provide necessary information for sensing retinal functional parameters such as retinal vessel oxygenation (sO_2) [9,10]. Mapping the retinal vessel sO_2 and imaging the retinal vasculature is important for the early diagnosis of diabetic retinopathy (DR), one of the leading blinding diseases around the world characterized by retinal blood vessel malfunctions [11].

Optical absorption can also provide specific contrast for imaging the pigmentation of retinal pigment epithelium (RPE), a monolayer of pigmented cells located between vessels of the choriocapillaris and light-sensitive outer segments of the photoreceptors. RPE has complex biological functions in the visual process including participation in the regeneration of retina in the visual cycle and the phagocytosis of photoreceptor outer segments; a failure of either of these functions can lead to degeneration of the retina, loss of visual function, and eventually blindness [12]. RPE cell malfunction contributes to numerous retinal diseases, including age-related macular degeneration (AMD), another leading blinding disease in industrialized countries. There have been considerable efforts in imaging the RPE, the most successful of which is lipofuscin autofluorescence imaging [13]; however, there still has been no technology that can directly image the optical absorption of the RPE.

Photoacoustic microscopy (PAM) [14–16] is an optical-absorption based microscopic imaging modality that detects laser-induced ultrasonic waves (photoacoustic or PA waves) as

a result of specific optical absorption. Since optical absorption is strongly associated with physiological parameters, PAM has drawn great interests from various biomedical research fields. If it can be adapted to retinal imaging, PAM has the potential to greatly improve the diagnosis and research of DR and AMD.

Our recent developments on the laser scanning optical-resolution PAM [17–19] and its integration with OCT have opened a window for photoacoustic ophthalmoscopy (PAOM). In this paper we report our latest progress on PAOM for *in vivo* retinal imaging in small animals.

2. Methods

Figure 1(a) shows a schematic of the experimental system. The illumination source was a frequency-doubled Q-switched Nd:YAG laser (SPOT-10-100-532, Elforlight Ltd, UK: 532 nm; 10 µJ/pulse**;** 2 ns pulse duration; 30 kHz pulse repetition rate). The output laser light was attenuated with a series of neutral density (ND) filters before coupled into a 2×2 single mode optical fiber beam splitter. The output laser light from one output arm of the beam splitter was collimated and combined with the OCT light beam in the sample arm by a dichroic mirror (FEL0700, Thorlabs, Inc). The other output arm of the fiber beam splitter was connected to a multimode fiber beam splitter, the outputs of which were connected to two photodiodes (DET10A, Thorlabs Inc), respectively. To ensure ocular laser safety, the PAOM laser pulse energy was set lower than 40 nJ/pulse.

The induced PA waves from the retina were detected by a custom-built needle ultrasonic transducer (30 MHz; bandwidth: 50%; active element diameter: 1 mm), which was placed in contact with the eyelid coupled by ultrasound gel [Fig. 1(b)]. The detected PA signals were first amplified by 80 dB then digitized and stored by a digitizer (PCI-5122, National Instruments) at a sampling rate of 100 MS/s. The energy of each laser pulse was also recorded by one of the photodiodes (Pd1) to compensate for the pulse energy instability. No signal averaging was used. The axial resolution of the PAOM was independently quantified to be 23 μm and the lateral resolution was comparable to that of the OCT subsystem (only differed by the ratio of the two optical wavelengths between PAOM and OCT).
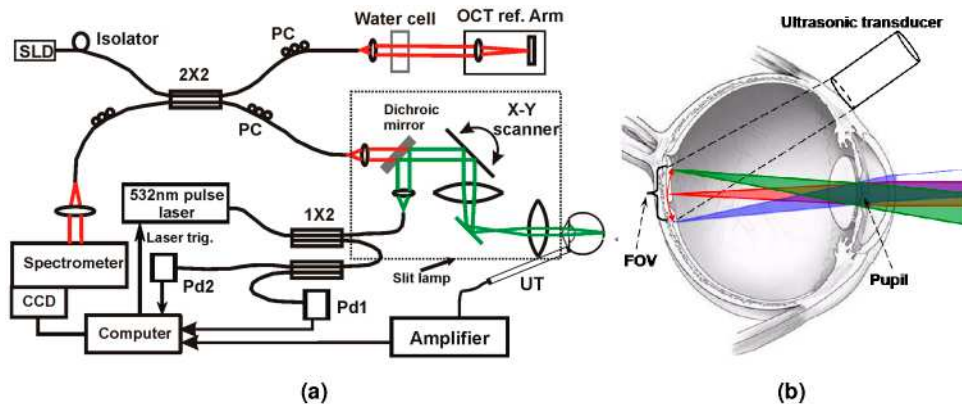

Fig. 1. Experimental system of the OCT-guided PAOM. (a) Schematic of the OCT-guided PAOM. (b) Illustration of the optical beam delivery to the retina and the position of the ultrasonic transducer. The light delivery systems were built on a slit-lamp bio-microscope. The two imaging subsystems are synchronized by the PAOM laser pulses detected by photodiode Pd1. SLD: superluminescent diode; PC: polarization controller; Pd: photodiode; FOV: field of view; UT: ultrasonic transducer.

The fiber-based spectral-domain OCT (SD-OCT) subsystem is similar to that reported in our previous publications [20]. Briefly, the SD-OCT consists of a superluminescent diode light source (IPSDM0821C-101, Inphenix), a 3-dB fiber coupler, a reference arm, a sample arm coupled with the PAOM, and a spectrometer for detecting the interference signals in the

spectral domain. The light source has a center wavelength of 870 nm and a full-width-half-maximum bandwidth of 100 nm. The exposure time of the line scan CCD camera (Aviiva, e2V, Chelmsford) in the spectrometer was set to 36 μs, which can acquire OCT images with a line rate of 24 kHz. The measured sensitivity was better than 95 dB. The calibrated depth resolution is 4 μm in tissue and the lateral resolution is estimated to be 20 μm. The combined PAOM and OCT light beams were scanned by an x-y galvanometer and delivered to the eye through an achromatic relay lens (f = 60 mm) and an objective lens (f = 14 mm, ACH 12.5×14 VIS-NIR, Edmund Industrial Optics).

To ensure automatic registration of the two imaging modalities as described in [18], the PAOM and OCT subsystems were synchronized by the sampling clock of the analogue output (AO) board (PCI-6731, National Instruments), which triggers both the PAOM laser and the image acquisition board for the CCD camera in the OCT spectrometer and controls the galvanometer scanner. The PAOM data acquisition was triggered by one of the photodiodes (Pd2) to avoid laser jittering.

We used Long Evans rats (body weight: 300 g, Charles Rivers) with normal retinas to assess the imaging capability of the multimodal system. The animals were anesthetized by intraperitoneal (IP) injection of a cocktail containing Ketamine (80 mg/kg body weight) and Xylazine (10 mg/kg body weight). In the meantime, the pupils were dilated with 10% Phenylephrine solution. Drops of artificial tears were applied to the animals' eyes every two minutes to prevent dehydration of the cornea and cataract formation. After anesthetization, the animals were restrained in a mounting tube, which was fixed on a five-axis platform. Raster scans with the fast axis along the horizontal direction were performed. The scan angle was approximately 20° for imaging the rat retina.

All experiments were performed in compliance with the guidelines of the University of Southern California's Institutional Animal Care and Use Committee.

3. Results and discussions

The OCT-guided PAOM has two operation modes: alignment mode and acquisition mode. At the beginning of each imaging session, the PAOM worked in the alignment mode and the PA laser was blocked. Only the real-time OCT display was activated to provide guidance for locating the retinal region of interest (ROI). After the ROI was indentified, the PAOM laser was turned on and the system was switched to acquisition mode. In both PAOM and OCT, the A-line rate was 24 kHz. For B-scan images consisting of 256 A-lines, the B-scan frame rate was 93 Hz. The simultaneous acquisition of the volumetric PAOM and OCT images consisting of 256 B-scans took 2.7 seconds.

Figure 2 shows the simultaneously acquired PAOM [Fig. 2(a)] and OCT [Fig. 2(b)] B-scan images of the left eye of a rat at the position marked in Fig. 2(c). As clearly seen in the PAOM B-scan, the blood vessels appear as clusters of high amplitude PA signals. Beneath the blood vessels, the continuous line of high PA amplitude is the RPE layer. The vertical lines mark the corresponding positions of the recognized vessels, which show the automatic registration of the two modalities. Figures 2(a) and 2(b) demonstrate the contrast mechanism of PAOM–the stronger the optical absorption, the stronger the generated ultrasonic signals. We can see that the hemoglobin in the blood vessels and the melanin in the RPE cells are strong absorbers of the illuminating light, while other retinal tissues have very low optical absorption. This difference in optical absorption provides the foundation of functional and anatomical imaging of the blood vessels and the RPE.

Figure 2(c) shows the maximum-amplitude-projection (MAP) of the PA data set. The circular boundary of RPE at the optic disc can be clearly observed. We can find that inside the optic disc only the blood vessels absorb the illuminating light; thus, the optic disc appears dark except for the blood vessels. The shadow marked HA in the MAP image is casted by the hyaloid artery remnant [8]. The signal-to-noise ratio in Fig. 2(c) is 23 dB.
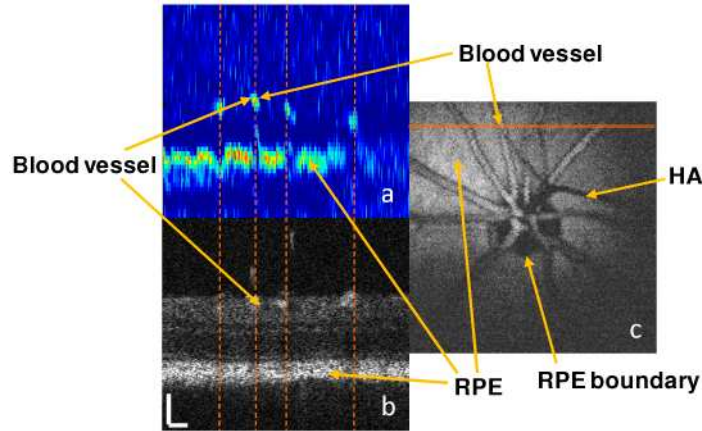
Fig. 2. Comparison of OCT and PAOM images acquired simultaneously *in vivo*. (a) PAOM B-scan image in pseudocolors; (b) OCT B-scan image; (c) MAP image of the PAOM data set. Bar: 100 µm.

It is important to note in Fig. 2(a) that the depth resolution of the current PAOM system is sufficient to resolve the retinal blood vessels from the RPE in the depth direction. This resolving capability guarantees no interference between the blood vessels and the RPE when quantitative absorption is calculated from the images, which is critical for calculating the blood vessel sO_2 from the PAOM image.

Figure 3 demonstrates the volumetric imaging capability of PAOM. Figure 3(a) is a movie visualizing the imaged retinal vessels and RPE from different viewing angles. The shadows on the RPE are created by blood vessels blocking the illuminating laser light. Moreover, we developed an algorithm [21] to automatically segment the RPE layer and the retinal vessels. Figure 3(b) shows the MAP image of the segmented blood vessels, and Fig. 3(c) shows the overlaid MAP image of the segmented retinal vessel onto the segmented RPE, where the vessels are pseudo-colored in red and the RPE is pseudo-colored in blue.
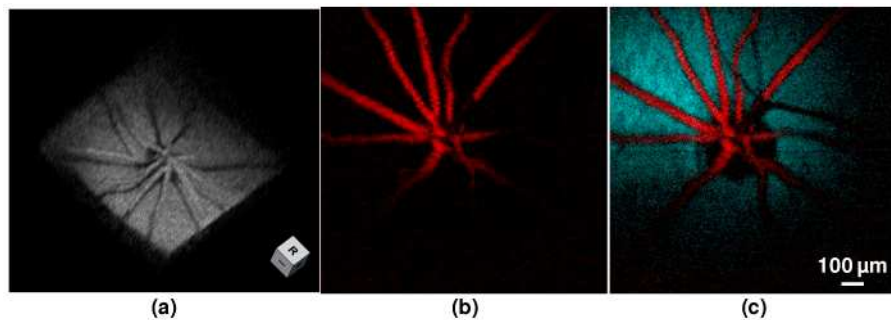

Fig. 3. Volumetric visualization and segmentation of PAOM image. (a) (Media 1) showing the imaged retinal structure by PAOM. (b) Segmented PAOM images of the retinal blood vessels. (c) Pseudo-colored PAOM images of the retinal vessels and RPE.

The field of view (FOV) of the PAOM was determined by the ultrasonic transducer, which had a circular area with a diameter of ~1 mm. By adjusting the orientation of the transducer we can target different retinal areas. The PA images of the same retina acquired at different transducer orientations can be montaged to form an image with larger FOV. Figure 4(a) shows a montage of two PAOM images of the same retina. The enlarged FOV covers both the superior and inferior areas of the retina compared with the FOV shown in Fig. 2(c). For comparison, Fig. 4(b) shows the fundus image constructed from the simultaneously acquired 3D OCT data set [20], where the blood vessels appear darker than

the RPE. The vessel structure imaged by both PAOM and OCT agree with each other, except the blood vessels inside the optic disc in the OCT fundus image are not as clear as in the PAOM.
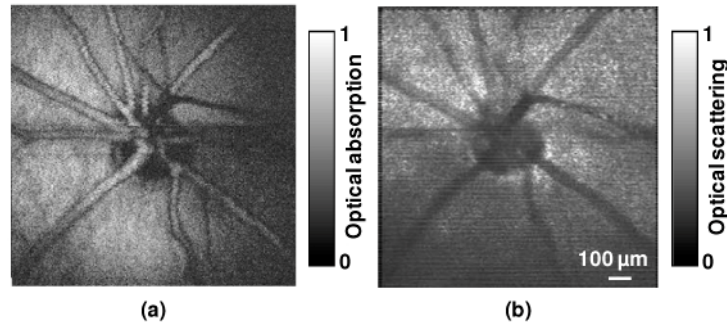

Fig. 4. (a) Montage of two PAOM images of the same rat retina. (b) OCT fundus image of the same retina. One of the two PAOM images has a FOV on the superior retina and the other has a FOV on the inferior retina. Bar: 100

Laser eye safety is one reasonable concern for *in vivo* retinal imaging. The design of the PAOM system strictly follows the ANSI laser safety standards [22]. The ocular maxim permissible exposure (MPE) depends on the optical wavelength, pulse duration, exposure duration, and exposure aperture. Signal averaging was not employed during data acquisition; thus, each scanning location on the retina was exposed to a single laser pulse. For a single laser pulse at 532 nm, the MPE should not exceed 5×10^{-7} J/cm^2; this requires the maximum pulse energy to be 0.2 µJ, assuming the size of a typical dilated human pupil to be 7 mm in diameter [20]. The laser pulse energy used in the experiments was only 0.04 µJ, which is within the ANSI laser safety limit. We also checked the same eye with a commercial retinal imaging machine (Spectralis, Heidelberg Engineering) two weeks after PAOM imaging. Using different modes of imaging (SLO, red free, and auto-fluorescence) no damage to the RPE and retinal blood vessels has been observed.

4. Conclusions

The successful imaging of the retinal vessels and RPE in rat eyes demonstrated the capability of the technology. Our current study laid the foundation for future quantitative imaging of the sO$_2$ of the retinal vessels (using multiple wavelength illumination sequentially [23]) and the distribution of the pigment in the RPE cell layer, which are important for the research and clinical diagnosis of DR and AMD (the two leading blinding diseases worldwide). The fast imaging speed (2.7 seconds for the whole 3D data acquisition), which is currently limited by the pulse repetition rate of the illuminating laser, makes the system suitable for routine *in vivo* applications in ophthalmic research.